International Journal of Engineering Research & Technology (IJERT)
ISSN: 2278-0181
Vol. 15 Issue 09 , September - 2026

3D Transient FEA Sensitivity Analysis of Unbalanced Magnetic Pull in Submersible Induction Motors Under Multi-Axis Manufacturing Tolerances and Axial Rotor Tilt Asymmetry

Dhyey Dudhat
M.Tech Student
Department of Mechanical Engineering
R. K. University, Rajkot

***Abstract* - Unbalanced Magnetic Pull (UMP) caused by dynamic rotor eccentricity is a primary driver of mechanical vibration, acoustic noise, and premature bushing failure in high aspect ratio submersible induction motors. Traditional two-dimensional (2D) finite element analysis (FEA) cannot capture three-dimensional (3D) spatial phenomena such as axial rotor tilting. This paper presents a 3D transient electromagnetic FEA sensitivity study evaluating the impact of multi-axis manufacturing tolerances on UMP dynamics in submersible induction machines. A 16-run full factorial Design of Experiments (DoE) matrix is implemented across four independent spatial coordinates bounded by an industrial machining tolerance window while evaluating a full scale model dimensions in calculation. Transient simulation results indicate that the nominal rotor configuration exhibits a stable steady state peak unbalanced magnetic pull (UMP) magnitude. Under extreme manufacturing tolerance conditions, a slight increase in the peak UMP magnitude is observed relative to the nominal configuration, demonstrating that rotor dimensional variations have a measurable but limited influence on electromagnetic force. Morris Method elementary main effect analysis identifies the top radial displacement as the primary contributor to variations in peak force magnitude, whereas bottom radial displacement has a greater influence on the mean force offset. Furthermore, the analysis reveals an axial tilt asymmetry, where opposing top and bottom rotor offsets produce higher magnetic force spikes than parallel rotor shifts. Maintaining rotor manufacturing tolerances within the specified allowable range limits UMP force degradation to a small level, thereby establishing a quantitative guideline for rotor quality control in submersible motors.**

Keywords - Submersible induction motors, Unbalanced Magnetic Pull (UMP), 3D transient FEA, manufacturing tolerances, axial rotor tilt asymmetry, Design of Experiments (DoE), sensitivity analysis.

I. INTRODUCTION

Submersible induction motors serve as the critical driving component in deep-well water extraction, offshore oil and gas recovery, subsea pumping, and industrial fluid transport. Unlike conventional surface mounted induction machines, submersible motors are characterized by an extremely high axial length-to-diameter ratio (L/D > 4), ultra-narrow radial airgaps to maximize torque density, and continuous operation in demanding underwater environments [1]. Due to these stringent mechanical constraints, even minor manufacturing imperfections can severely compromise operational reliability [2]. Among various mechanical and electromagnetic anomalies, Unbalanced Magnetic Pull (UMP) caused by rotor dynamic eccentricity is recognized as a primary driver of operational degradation [3]. Dynamic eccentricity occurs when the rotor center of rotation deviates from its geometric axis, causing the airgap length to vary periodically during rotation [4]. This asymmetric airgap distribution alters local magnetic flux densities, producing a net transverse electromagnetic force vector directed toward the narrowest airgap region [5]. Under high load conditions, persistent UMP exerts severe cyclic fatigue on rotor bushings and can trigger rotor stator rub [6].

A. Literature Review & Research Gap

Numerous studies have focused on modeling and mitigating UMP in induction machines. Early analytical formulations established fundamental relations linking radial airgap asymmetry to harmonic force frequencies [8] [9]. With the advent of modern computational tools, two-dimensional (2D) transient Finite Element Analysis (FEA) became the standard approach for evaluating local saturation, slot harmonics, and non-linear UMP behavior under dynamic eccentricity [9] [10] [11]. However, existing literature exhibits a fundamental limitation: the majority of UMP studies rely on 2D FEA approximations.

A 2D FEA model implicitly assumes that rotor eccentricity remains perfectly uniform across the entire axial stack length of the machine [12]. While this assumption may hold for short-stack surface motors, it fails entirely for high-aspect-ratio submersible motors. In actual factory manufacturing and assembly, machining tolerances at the top and bottom bushing (x_{top}, x_{bot}, y_{top}, y_{bot}) occur independently [13]. Consequently, real-world manufacturing variations introduce spatial 3D axial rotor tilting, where the rotor axis inclination creates non-uniform airgap variations along the z-axis [14]. Standard 2D

International Journal of Engineering Research & Technology (IJERT)
ISSN: 2278-0181
Vol. 15 Issue 09 , September - 2026

numerical frameworks cannot capture spatial tilt dynamics. Furthermore, we have also added the shifting of the co-ordinates to the industrial machining tolerances used in manufacturing process to get study close to the practical world.

II. 3D FEA Model Setup and Machine Specifications

A. Machine Geometry, Bushing Layout, and Materials

The electric machine investigated in this study is a 40 HP (29.83kW), 2-pole, 415 V, 50 Hz delta-connected submersible induction motor. Initial electromagnetic sizing, slot profiles, and winding distribution were designed using ANSYS RMexpert, while full 3D transient electromagnetic simulations were executed in ANSYS Maxwell 3D [15]. To optimize computational efficiency for the 3D transient solutions, an FEA sector model was implemented.

The machine features a stator inner diameter of D_{si}= 70.0 mm and a rotor outer diameter of D_{ro}=69.0mm, with radial airgap of 0.5mm. Both the stator and rotor lamination core stacks extend axially over L_{stack}= 700.0mm, which is a high aspect ratio of L/D_{st}= 10.0. To model realistic mechanical assembly, a user defined coordinate system is established where the origin (z = 0mm) is placed at the physical bottom face of the stator core stack. The active magnetic laminations of the stator and rotor span axially from Z=0mm to z=700.0mm. The bushing of motor is located at Z=-350.0mm at lower surface and Z=+1100.0mm with respect origin. The stator and rotor cores are constructed from high-permeability Cogent Power - M1000-100A non-oriented electrical silicon steel. The rotor conductive cage circuit comprising the 28 rotor bars and both short circuiting end-rings is modeled using Electrical Conductor (EC) Grade Pure Copper (99.98% purity).

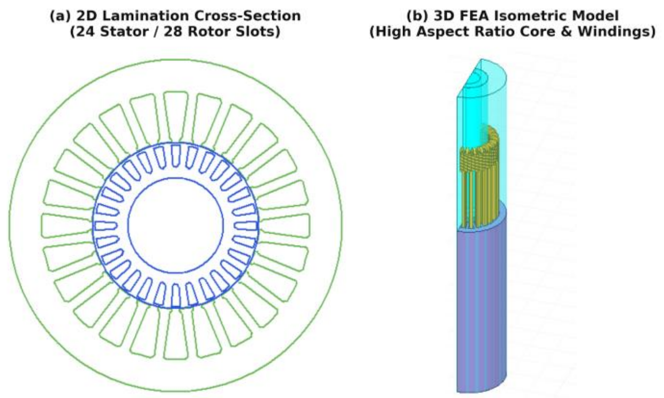

Fig. 1 Electric induction motor design model: (a) 2D cross-sectional view showing stator and rotor slot lamination profiles, (b) 3D sector model.

TABLE I: Motor Geometry, Material, and Mechanical Parameters

Parameter Category	Design Parameter	Symbol	Input Value	Physical Unit
Operating Rating	Rated Output Power	P_n	40(29.83)	HP(KW)
	Rated line to line Voltage	V_n	415	V(rms)
	Phase Winding Connection	Δ	Delta	-
	Rated Supply Frequency	f	50	Hz
	Number of Poles	p	2	-
	Synchronous Speed	n_s	3000	RPM
	Rated Mechanical Speed	n_r	2900	RPM
	Thermal Operating Temperature	T_{op}	75	^{0}C
Stator Geometry	Stator Outer Diameter	D_{so}	138	mm
	Stator Inner Diameter	D_{si}	70	mm
	Stator Lamination Steel	-	Cogent Power – M1000-100A	-
	Stator no. of Slots	S_1	24	-
Rotor Geometry	Rotor Outer Diameter	D_{ro}	69	mm
	Rotor Inner Shaft Diameter	D_{ri}	40	mm
	Nominal Radial AirGap	g_0	0.5	mm
	Core Length	L_{stack}	700	mm
	Aspect Ratio	L/D_{st}	10	-
	Number of Rotor Slots	S_2	28	-
	Rotor Core Material	-	Cogent Power – M1000-100A	-
	Rotor Cage and Rotor	-	EC Grade Pure Copper	-
Bushing Co-ordinates	Co-ordinate of Origin	Z_0	Base of Stator Core Stack	-
	Lower Shaft Bushing Location	$Z_{bush, lower}$	-350.0(from origin)	mm
	Upper Shaft Bushing Location	$Z_{bush ,upper}$	+1100.0(from origin)	mm
	Machining Tolerance	±	±0.0125(radially)	mm

B. Electromagnetic Field Governing Equations

To analyze three-dimensional magnetic flux distribution, non-linear core saturation, and transient current generation within ANSYS Maxwell 3D, the low-frequency Maxwell equations are solved using the Magnetic Vector Potential (A) and Electric Scalar Potential (φ) formulation (A- φ).

In a high-aspect-ratio 3D motor model, magnetic flux does not travel exclusively in two-dimensional radial planes; flux lines twist around slot openings, leak axially around the copper end-rings, and vary along the 700.0mm stack length. To capture this 3D spatial field mathematically, the magnetic flux density vector (B) is expressed as the spatial curl of a magnetic vector potential A, such that B=∇×A. This formulation enforces magnetic field continuity throughout the machine volume. Within conductive motor regions specifically the EC grade copper rotor bars, copper end-rings, and silicon steel core laminations changing magnetic flux induces secondary voltages and eddy currents. The governing differential equation in these conductive domains is:

$$\nabla \times \left(\frac{1}{\mu} \nabla \times A\right) = J_e - \sigma \frac{\partial A}{\partial t} - \sigma \nabla \varphi \quad (1)$$

where:

International Journal of Engineering Research & Technology (IJERT)
ISSN: 2278-0181
Vol. 15 Issue 09 , September - 2026

- A is the 3D Magnetic Vector Potential (Wb/m).
- Φ is the Electric Scalar Potential (V).
- J_e is the applied external source current density vector (A/m^2).
- μ is the non-linear magnetic permeability (H/m) of the Cogent Power - M1000-100A steel core.
- σ is the material electrical conductivity (S/m) (for EC grade pure copper, $\sigma_{75°C} \approx 4.77\times10^7$S/m).
- $\frac{\partial A}{\partial t}$ is the time derivative of the magnetic potential, which induces physical electromotive force (EMF).

In non-conductive domains including the 0.50mm radial airgap and surrounding exterior air space electrical conductivity drops to zero (σ = 0). No induced eddy currents can flow through the air, simplifying the field governing equation to:

$$\nabla \times \left(\frac{1}{\mu_0}\nabla \times A\right) = 0 \qquad (2)$$

where $\mu_0 = 4\pi\times10^{-7}$ H/m is the magnetic permeability of free space.

Once the local magnetic vector potential A is resolved across the 3D mesh, the localized magnetic flux density vector B = (B_r, B_θ, B_z) is extracted throughout the airgap volume. The net electromagnetic force acting on the rotor structure is calculated using the Maxwell Stress Tensor. Conceptually, Maxwell stress models magnetic flux lines as elastic lines under physical tension where magnetic flux lines concentrate tightly in narrow airgap zones, they exert a localized tensile force pulling the iron surfaces together. To determine the net instantaneous Unbalanced Magnetic Pull vector (F_{UMP}) acting across the active 700.0mm core length, the stress tensor is integrated over an imaginary cylindrical mid-airgap surface S_{gap} located at radius r = 34.75mm:

$$F_{UMP}(t) = \frac{1}{\mu_0}\iint_{S_{gap}} \left[(B\cdot n)B - \frac{1}{2}B^2 n\right] dS \qquad (3)$$

where:

- $F_{UMP}(t)$ is the net 3D Unbalanced Magnetic Pull force vector (N), decomposed into Cartesian force components (F_x, F_y, F_z).
- B is the local instantaneous magnetic flux density vector (T) at each surface element.
- n is the outward normal unit vector pointing from the rotor surface toward the stator bore.
- B = |B| is the overall scalar flux density magnitude (T)
- dS are the incremental surface area element (m^2) integrated along the full 700.0mm cylindrical airgap length.

This stress tensor integration tracks how spatial airgap variations alter the magnitude, rotational trajectory, and peak spikes of the magnetic forces pulling on the motor rotor.

C. Meshing and Time-Step Solver Setup

To capture magnetic flux accurately where forces are calculated, the 0.50 mm airgap volume is split into three concentric cylindrical layers:

1. **Stator Airgap Layer:** A fixed mesh layer attached to the inner stator bore.
2. **Sliding Band Surface:** A rotating interface located at the mid-airgap radius (r = 34.75mm). This surface rotates dynamically with the rotor at its rated speed of 2900 RPM.
3. **Rotor Airgap Layer:** A rotating mesh layer attached directly to the outer surface of the copper-bar rotor core.

To ensure the mesh density was sufficient, adaptive mesh refinement was applied in ANSYS Maxwell 3D. The mesh was refined step-by-step until the calculated electromagnetic torque and magnetic force values stopped changing, confirming mesh independence. The transient simulation is solved in the time domain from t = 0.0s to t = 0.15s (150ms total time) using a fixed time step of 0.001s. At a supply frequency of 50 Hz, one electrical AC cycle lasts 0.02s(20ms). A time step of 0.001s provides 20 discrete evaluation points per AC cycle. This resolution captures both the slow mechanical speed changes during motor startup and the fast 50 Hz electromagnetic force oscillations.

D. Baseline Model Performance

To establish a clear benchmark, the nominal baseline model where the rotor is perfectly centered ($x_{top} = x_{bot} = y_{top} = y_{bot}$ = 0.0mm) was simulated across the full 0.0s to 0.15s time window. When the motor starts at t = 0.0s, currents and magnetic force fluctuations occur as the shaft accelerates up to speed. By t = 0.10s (100ms), these initial starting transients die out, and the machine enters smooth, steady-state operation. The 3-phase currents settle into balanced sinusoidal AC waves across all three delta-connected phases. The rotor stabilizes at its rated operational speed of 2900 RPM.

During the steady-state window (0.10s to 0.15s), the magnetic pull forces acting on the baseline rotor are evaluated:

1) Baseline Peak UMP ($F_{peak, base}$) = 11.48kN (11,482.05N)
2) Baseline Mean UMP ($F_{mean, base}$) = 6.66kN (6,664.44N)

In simple 2D motor models, a perfectly centered rotor theoretically produces zero net magnetic pull. However, in this realistic 3D model, three physical factors create a baseline force of 11.48kN. The magnetic interactions between the 24 stator slots and 28 rotor slots create small local magnetic variations as the slots pass each other. Magnetic flux leaks outward around the pure EC copper end-rings at both the top (z = 700.0mm) and bottom (z= 0.0mm) ends of the active core stack. Additionally, because a sector model is utilized to maintain 3D transient FEA computational feasibility. This 11.48kN peak force serves as our baseline reference value.

III. MULTI-AXIS TOLERANCES & DOE SETUP

A. Multi-Axis Spatial Coordinate Model

In conventional two-dimensional (2D) FEA studies, rotor eccentricity is assumed to be uniform along the entire length of the machine core. A 2D model implicitly treats the rotor as a rigid cylinder that only moves parallel to the stator bore. In actual factory manufacturing, machining, and bushing assembly, however, manufacturing errors occur independently at both ends of the shaft. To capture realistic three-dimensional (3D)

International Journal of Engineering Research & Technology (IJERT)
ISSN: 2278-0181
Vol. 15 Issue 09 , September - 2026

manufacturing variations, the spatial position of the rotor axis is defined using four independent Cartesian coordinates at the bushing position. Because the mechanical shaft acts as a rigid beam over the active magnetic core length, the radial offset at any intermediate axial position z is governed by linear spatial interpolation:

$$x(z) = x_{bot} + \frac{z - z_{bush,\ lower}}{z_{bush,\ upper} - z_{bush,\ lower}} \left(x_{top} - x_{bot} \right) \quad (4)$$

$$y(z) = y_{bot} + \frac{z - z_{bush,\ lower}}{z_{bush,\ upper} - z_{bush,\ lower}} \left(y_{top} - y_{bot} \right) \quad (5)$$

This 4-variable spatial coordinate model allows us to distinguish two fundamental types of mechanical displacement:

1. **Pure Parallel Shift:** Occurs when the top and bottom bushing offsets are identical in magnitude and direction ($x_{top} = x_{bot}$ and $y_{top} = y_{bot}$). In this case, the airgap decreases uniformly along the entire 700.0mm stack length.
2. **Axial Rotor Tilt Asymmetry:** Occurs when the top and bottom offsets move in opposite directions ($x_{top} = -x_{bot}$ or $y_{top} = -y_{bot}$). In this condition, the rotor center line tilts spatially relative to the stator bore, causing the narrowest airgap point at z = 700.0 mm to be located on the opposite side of the machine relative to z = 0.0mm.

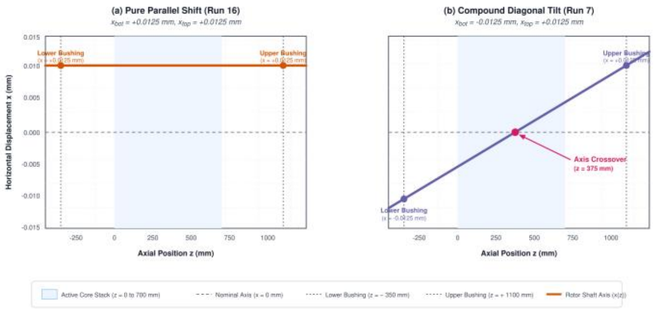

Fig. 2 Comparison of rotor arrangement modes across the active core stack: (a) parallel offset (Run 16) resulting in uniform axial airgap reduction, and (b) diagonal axis tilt (Run 7) exhibiting axis crossover and variation of airgap at core ends.

B. *Design of Experiments (DoE) Matrix*

To evaluate how independent spatial variations across the four bushing coordinates (x_{top}, x_{bot}, y_{top}, y_{bot}) affect UMP dynamics, a full factorial Design of Experiments (DoE) approach is implemented. In a full factorial experiment, every possible combination of variable settings is evaluated. Since there are four independent spatial variables (k = 4) and each variable is tested at two discrete levels a low level of -0.0125mm and a high level of +0.0125mm the total number of required FEA simulation runs is $2^k = 2^4 = 16$ runs [16].

TABLE II: Full Factorial Design of Experiments (DoE) Parameter Matrix

Run	x_{bot} (mm)	x_{top} (mm)	y_{bot} (mm)	y_{top} (mm)	Physical movement type
Run 0 (Base)	0	0	0	0	Perfectly Centered Baseline Reference
Run 1	−0.0125	−0.0125	−0.0125	−0.0125	Pure Diagonal Parallel Shift
Run 2	−0.0125	−0.0125	−0.0125	+0.0125	y-Axis Tilt with x-Parallel Offset
Run 3	−0.0125	−0.0125	+0.0125	−0.0125	Opposing y-Axis Tilt with x-Parallel Offset
Run 4	−0.0125	−0.0125	+0.0125	+0.0125	y-Axis Parallel Shift with x-Parallel Offset
Run 5	−0.0125	+0.0125	−0.0125	−0.0125	x-Axis Tilt with y-Parallel Offset
Run 6	−0.0125	+0.0125	−0.0125	+0.0125	Dual-Axis Compound Tilt (x and y)
Run 7	−0.0125	+0.0125	+0.0125	−0.0125	Dual-Axis Opposing Tilt
Run 8	−0.0125	+0.0125	+0.0125	+0.0125	x-Axis Tilt with y-Parallel Shift
Run 9	+0.0125	−0.0125	−0.0125	−0.0125	Opposing x-Axis Tilt with y-Parallel Offset
Run 10	+0.0125	−0.0125	−0.0125	+0.0125	Dual-Axis Opposing Tilt
Run 11	+0.0125	−0.0125	+0.0125	−0.0125	Dual-Axis Compound Tilt (x and y)
Run 12	+0.0125	−0.0125	+0.0125	+0.0125	x-Axis Tilt with y-Parallel Shift
Run 13	+0.0125	+0.0125	−0.0125	−0.0125	x-Axis Parallel Shift with y-Parallel Offset
Run 14	+0.0125	+0.0125	−0.0125	+0.0125	y-Axis Tilt with x-Parallel Shift
Run 15	+0.0125	+0.0125	+0.0125	−0.0125	Opposing y-Axis Tilt with x-Parallel Shift
Run 16	+0.0125	+0.0125	+0.0125	+0.0125	Pure Diagonal Parallel Shift

C. *Sensitivity Analysis Formulation (Morris Method)*

To quantify which of the four bushing coordinates has the largest impact on Unbalanced Magnetic Pull, a main effect sensitivity analysis based on the Morris Method is applied. The Morris Method evaluates the Elementary Effect (E_i) of changing an individual input coordinate i from its low level (-0.0125mm) to its high level (+0.0125mm) while holding other parameters constant:

$$E_i = \frac{Y(x_1, .., x_i + \Delta, .., x_4) - Y(x_1, .., x_i, .., x_4)}{\Delta} \quad (6)$$

where:

- E_i is the elementary sensitivity coefficient for spatial coordinate i (where i ∈ (x_{top}, x_{bot}, y_{top}, y_{bot})).
- Y is the output performance metric extracted from the 3D transient FEA solution. Two specific metrics are evaluated:

International Journal of Engineering Research & Technology (IJERT)
ISSN: 2278-0181
Vol. 15 Issue 09 , September - 2026

1. **Steady-State Peak UMP (F_{peak}):** The maximum magnitude of the UMP vector during settled operation (0.10s to 0.15s).
2. **Steady-State Mean UMP (F_{mean}):** The average magnitude of the UMP vector during settled operation (0.10s to 0.15s).

- Δ is the step change across the manufacturing tolerance window:

$$\Delta = (+0.0125mm) - (-0.0125mm) = 0.0250mm$$

A larger absolute value $|E_i|$ indicates that small machining errors at coordinate i cause large increases in magnetic force. Comparing the relative magnitudes of $|E_{x, top}|$, $|E_{x, bot}|$, $|E_{y, top}|$ and $|E_{y, bot}|$ allows us to rank the coordinates in order of importance, providing motor manufacturers with guidance on which shaft dimensions require the tightest machining control.

IV. Transient Simulation Results, Sensitivity Analysis, and Discussion

A. Transient FEA Results and DoE Force Waveband

All 16 full-factorial Design of Experiments (DoE) runs and the centered baseline reference model (Run 0) were simulated in ANSYS Maxwell 3D over a total transient time domain of t = 0.0ms to 150.0ms. To eliminate initial electrical starting and mechanical speed ramping, all steady-state force metrics were extracted during the settled steady-state operating window between t=100.0ms and 150.0ms. Across the entire manufacturing tolerance matrix, the resultant magnitude of the Unbalanced Magnetic Pull (mag(F_x)) exhibits a tightly bounded waveband:

- Nominal Baseline Peak UMP (Run 0): 11.48kN (11,482.05N)
- Nominal Baseline Mean UMP (Run 0): 6.66kN (6,664.44N)
- Worst-Case Peak UMP (Run 7): 11.65kN (11,646.14N)
- Maximum Peak Force Increase: +164.09N (+1.43% increase relative to the perfectly centered baseline)
- Minimum Peak UMP (Run 13): 11.47kN (11,471.32N, a -0.09% change relative to baseline)

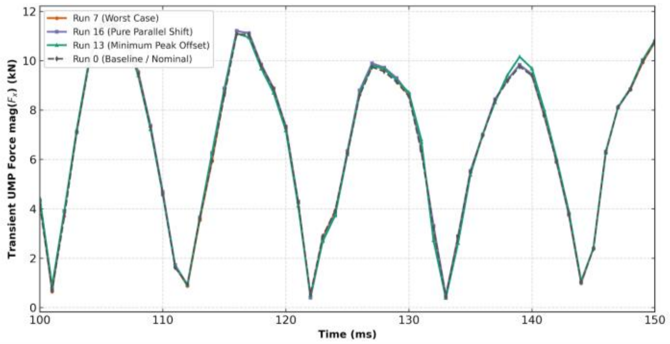

Fig. 3 Comparison of transient horizontal UMP force mag(F_x) over the steady-state evaluation window (100-150 ms) across nominal (Run 0), parallel shift (Run 16), worst case (Run 7), and minimum peak offset (Run 13).

This bounded behavior confirms that restricting bushing manufacturing tolerances within Δ_{tol} = ±0.0125mm successfully contains maximum dynamic UMP force amplification to under 1.5%.

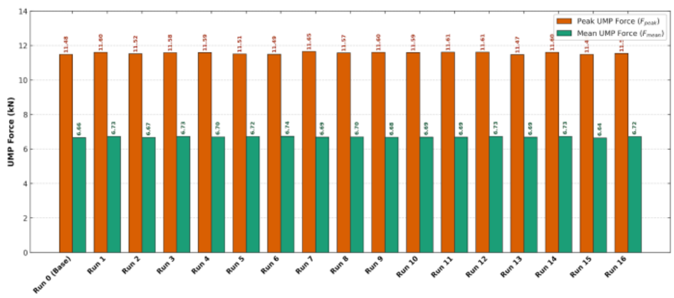

Fig. 4 Peak and mean UMP force magnitudes (F_{peak} and F_{mean}) across all Design of Experiments (DoE) rotor misalignment runs.

TABLE III: Evaluated Steady-State UMP Force Metrics Across DoE Runs (100ms-150ms)

Run	x_{bot} (mm)	x_{top} (mm)	y_{bot} (mm)	y_{top} (mm)	Peak UMP F_{peak} (kN)	Mean UMP F_{mean} (kN)	Peak Change vs. Base (%)
Run 0 (Base)	+0.0000	+0.0000	+0.0000	+0.0000	11.48	6.66	+0.00%
Run 1	−0.0125	−0.0125	−0.0125	−0.0125	11.6	6.73	+1.02%
Run 2	−0.0125	−0.0125	−0.0125	+0.0125	11.52	6.67	+0.34%
Run 3	−0.0125	−0.0125	+0.0125	−0.0125	11.58	6.73	+0.88%
Run 4	−0.0125	−0.0125	+0.0125	+0.0125	11.59	6.7	+0.91%
Run 5	−0.0125	+0.0125	−0.0125	−0.0125	11.51	6.72	+0.23%
Run 6	−0.0125	+0.0125	−0.0125	+0.0125	11.49	6.74	+0.05%
Run 7	−0.0125	+0.0125	+0.0125	−0.0125	11.65	6.69	+1.43%
Run 8	−0.0125	+0.0125	+0.0125	+0.0125	11.57	6.7	+0.75%
Run 9	+0.0125	−0.0125	−0.0125	−0.0125	11.6	6.68	+1.06%
Run 10	+0.0125	−0.0125	−0.0125	+0.0125	11.59	6.69	+0.91%
Run 11	+0.0125	−0.0125	+0.0125	−0.0125	11.61	6.69	+1.11%
Run 12	+0.0125	−0.0125	+0.0125	+0.0125	11.61	6.73	+1.13%
Run 13	+0.0125	+0.0125	−0.0125	−0.0125	11.47	6.69	−0.09%
Run 14	+0.0125	+0.0125	−0.0125	+0.0125	11.6	6.73	+1.02%
Run 15	+0.0125	+0.0125	+0.0125	−0.0125	11.48	6.64	−0.05%
Run 16	+0.0125	+0.0125	+0.0125	+0.0125	11.54	6.72	+0.51%

B. Sensitivity Analysis

To quantify the individual influence of each bushing coordinate (x_{top}, x_{bot}, y_{top}, y_{bot}) on peak magnetic pull force, a sensitivity analysis based on the Morris Method Elementary Effects was calculated across the 16-run factorial matrix [17]. The step change across the tolerance band is Δ=0.0250mm. Evaluating

International Journal of Engineering Research & Technology (IJERT)
ISSN: 2278-0181
Vol. 15 Issue 09 , September - 2026

the absolute mean elementary effect across matching coordinate pairs yields the quantitative impact per millimeter of bushing offset:

- Top Radial Displacement (x_{top}) Dominant Influence:

$$\mu^*_{x,top} = 69.14N\ (\frac{\mu^*}{\Delta} = 2765.76\frac{N}{mm})$$

- Bottom Radial Displacement (x_{bot}):

$$\mu^*_{x,bot} = 58.41N\ (\frac{\mu^*}{\Delta} = 2336.43\frac{N}{mm})$$

- Bottom Transverse Displacement (y_{bot}):

$$\mu^*_{y,bot} = 49.08N\ (\frac{\mu^*}{\Delta} = 1963.37\frac{N}{mm})$$

- Top Transverse Displacement (y_{top}):

$$\mu^*_{y,top} = 49.04N\ (\frac{\mu^*}{\Delta} = 1961.80\frac{N}{mm})$$

The top horizontal coordinate (x_{top}) exerts the strongest overall impact on peak magnetic force spikes during transient operation. The fundamental physical cause behind the heightened sensitivity of top bushing coordinates (x_{top}) relates directly to the asymmetrical mechanical positioning of the bushes relative to the active stack.

C. *Physical Mechanism of Axial Rotor Tilt Asymmetry*

The 3D transient FEA results highlight a clear difference in how the electric motor behaves under uniform parallel displacement versus complex spatial tilt. Under uniform parallel displacement when the rotor shifts evenly at both top and bottom bushing, the rotor remains perfectly parallel to the stator bore. The airgap narrows uniformly along the entire stack length, producing a peak Unbalanced Magnetic Pull (UMP) force of 11.54kN (+0.51% above baseline). Conversely, under compound spatial tilt (e.g., Run 7), the top and bottom bushing shift in opposing directions, causing the rotor axis to tilt diagonally across the stator bore. This generates the worst-case peak UMP force of 11.65kN (+1.43% or +164.09 N higher than baseline).

Three core physical drivers explain why axial rotor tilting amplifies magnetic pull forces significantly more than parallel shifts:

1. **Localized Airgap Narrowing:** When the rotor tilts, the airgap is no longer uniform along its length. Instead, it becomes tightest at the extreme top and bottom ends of the active magnetic core (z = 0.0mm and z = 700.0mm). At these outer stack edges, the localized radial gap narrows to its minimum possible distance, creating localized points of high magnetic force.
2. **Non-Linear Force Concentration:** Magnetic pull force does not increase linearly as the airgap closes it grows exponentially with the inverse square of the airgap distance. Because of this non-linear behavior, the strong magnetic pull generated at the tightly pinched ends of the core easily outweighs any force reduction at the wider regions. This creates a higher overall net dynamic force spike on the shaft.
3. **Asymmetrical Support:** The physical position of the lower bushing bush below the active stack (z = -350.0mm) creates an asymmetrical lever arm across the magnetic core (z = 0.0mm to 700.0mm).

D. *Manufacturing Quality Control and Design Recommendations*

The primary finding from the full-factorial FEA matrix is the validation of the selected manufacturing tolerance boundary. Restricting bushing offsets within this window successfully limits peak Unbalanced Magnetic Pull (UMP) force growth to a maximum of +1.43%. This tight force band confirms that cylindrical grinding and machining tolerances are entirely sufficient to prevent severe electromagnetic force amplification, demonstrating that further tightening of global tolerances across all coordinates is unnecessary for operational stability [18].

However, manufacturing quality control efforts should not be distributed equally across all coordinates; instead, inspection protocols must prioritize the top bushing side. Consequently, inspections and shop-floor machining tolerances should be specifically tightened on top side, as suppressing deviations at this specific coordinate provides the highest marginal reduction in transient magnetic force spikes.

V. CONCLUSION

A. *Summary of Findings*

This study presented a 3D transient electromagnetic finite element analysis (FEA) to evaluate the impact of bushing misalignments on Unbalanced Magnetic Pull (UMP) in an electric motor with asymmetrical bushing support positioning. By executing a 2^4 full-factorial Design of Experiments (DoE) matrix across top and bottom bushing coordinates, the dynamic force response was quantified during steady-state operation. The primary conclusion is that maintaining manufacturing tolerances within $\Delta = \pm 0.0125$mm successfully restricts UMP peak force variations to a narrow waveband. These findings confirm that standard precision cylindrical grinding capabilities are fully sufficient to stabilize transient magnetic pull without requiring overly restrictive manufacturing tolerances.

B. *Engineering Recommendations and Future Scope*

Machine shop inspection protocols should selectively tighten tolerances on the top bushing while maintaining standard tolerances on lower bushing coordinates, optimizing manufacturing yield while minimizing force spikes. Dial-indicator concentricity alignment should be mandatorily performed between lower and upper bushing housings prior to casing bolt down to prevent severe dual axis angular rotor tilting. Subsequent studies will extend this FEA framework by incorporating thermo-mechanical frame expansion, full 360° circumferential 3D FEM analysis, and structural rotor dynamics into a fully coupled multiphysics transient solver.

REFERENCES

[1] P. von Baeckmann, *Submersible Motor Dynamics and Electromechanical Modeling*, 2nd ed. Berlin, Germany: Springer-Verlag, 2019.

International Journal of Engineering Research & Technology (IJERT)
ISSN: 2278-0181
Vol. 15 Issue 09 , September - 2026

[2] H. Zhao, L. Zhang, and X. Liu, "Impact of precision machining tolerances on airgap uniformity in electrical machines," *CIRP Annals - Manufacturing Technology*, vol. 71, no. 1, pp. 481–484, 2022.

[3] A. Tenhunen, "Electromagnetic forces in induction machines," Ph.D. dissertation, Dept. Elect. Eng., Helsinki Univ. of Technology, Espoo, Finland, 2003.

[4] S. Nandi, H. A. Toliyat, and X. Li, "Condition monitoring and fault diagnosis of electrical machines—A review," *IEEE Transactions on Energy Conversion*, vol. 20, no. 4, pp. 719–729, Dec. 2005.

[5] B. Heller and V. Hamata, *Unbalanced Magnetic Pull in Electrical Machines*. Amsterdam, The Netherlands: Elsevier Scientific Publishing Company, 1977.

[6] M. K. Ghosh and R. Kumar, "Bearing fatigue and dynamic wear under unbalanced magnetic pull in heavy-duty electric drives," *Wear*, vol. 450–451, Art. no. 203250, Jun. 2020.

[7] J. Fruchtenicht, H. Jordan, and H. O. Seinsch, "Effects of airgap eccentricity on the operational behavior of three-phase induction motors," *Archiv für Elektrotechnik*, vol. 65, no. 1, pp. 19–29, Jan. 1982.

[8] D. G. Dorrell, "Analytical modeling of unbalanced magnetic pull in cage induction motors," *IEEE Transactions on Industry Applications*, vol. 33, no. 5, pp. 1241–1249, Sep./Oct. 1997.

[9] X. Chen, Y. Wang, and Z. Q. Zhu, "2D transient finite element analysis of unbalanced magnetic pull in induction motors with rotor eccentricity," *IEEE Transactions on Magnetics*, vol. 52, no. 7, Art. no. 8104504, Jul. 2016.

[10] Y. Park, S. B. Lee, and M. G. Melero, "Online rotor fault diagnosis and dynamic eccentricity monitoring in induction motors," *IEEE Transactions on Industrial Electronics*, vol. 66, no. 9, pp. 7231–7240, Sep. 2019.

[11] Z. Zhang, C. Gerada, and M. Galea, "Slot harmonic effects on unbalanced magnetic pull in high-utilization electrical machines," *IEEE Transactions on Energy Conversion*, vol. 36, no. 3, pp. 2145–2154, Sep. 2021.

[12] R. Islam, I. Husain, and A. Fardoun, "Comparative evaluation of 3D and 2D transient FEA for localized airgap magnetic pull in slender rotors," *IEEE Transactions on Industry Applications*, vol. 53, no. 4, pp. 3412–3420, Jul./Aug. 2017.

[13] A. Tenconi, S. Vaschetto, and A. Vigliani, "Electrical machines for automotive applications: How to deal with rotor eccentricity," *IEEE Transactions on Industry Applications*, vol. 50, no. 3, pp. 1820–1828, May/Jun. 2014.

[14] K. Ramesh and B. S. Raj, "Spatial rotor misalignment and dynamic force characteristics in submersible pump motor units," *Mechanical Systems and Signal Processing*, vol. 184, Art. no. 109712, Feb. 2023.

[15] S. J. Salon, *Finite Element Analysis of Electrical Machines*. Boston, MA, USA: Springer US, 1995.

[16] D. C. Montgomery, *Design and Analysis of Experiments*, 9th ed. Hoboken, NJ, USA: John Wiley & Sons, 2017.

[17] M. D. Morris, "Factorial sampling plans for preliminary computational experiments," *Technometrics*, vol. 33, no. 2, pp. 161–174, May 1991.

[18] Geometrical product specifications (GPS) — ISO code system for tolerances on linear sizes — Part 1: Basis of tolerances, deviations and fits, ISO Standard 286-1:2010, International Organization for Standardization, Geneva, Switzerland, 2010.